Annals of Biomedical Engineering
https://doi.org/10.1007/s10439-023-03211-3

S.I.: ELECTROPORATION FOR MEDICAL APPLICATIONS AND BIOTECHNOLOGY

Cytoskeletal Remodeling and Gap Junction Translocation Mediates Blood–Brain Barrier Disruption by Non-invasive Low-Voltage Pulsed Electric Fields

Neeraj Raghuraman Rajagopalan[1] · William-Ray Vista[2] · Masashi Fujimori[2,8] · Laurien G. P. H. Vroomen[3] · Juan M. Jiménez[1] · Niranjan Khadka[4,5,6] · Marom Bikson[6] · Govindarajan Srimathveeravalli[1,7]

Received: 28 December 2022 / Accepted: 14 April 2023

Abstract

High-voltage pulsed electric fields (HV-PEF) delivered with invasive needle electrodes for electroporation applications is known to induce off-target blood–brain barrier (BBB) disruption. In this study, we sought to determine the feasibility of minimally invasive PEF application to produce BBB disruption in rat brain and identify the putative mechanisms mediating the effect. We observed dose-dependent presence of Evans Blue (EB) dye in rat brain when PEF were delivered with a skull mounted electrode used for neurostimulation application. Maximum region of dye uptake was observed while using 1500 V, 100 pulses, 100 µs and 10 Hz. Results of computational models suggested that the region of BBB disruption was occurring at thresholds of 63 V/cm or higher; well below intensity levels for electroporation. In vitro experiments recapitulating this effect with human umbilical vein endothelial cells (HUVEC) demonstrated cellular alterations that underlie BBB manifests at low-voltage high-pulse conditions without affecting cell viability or proliferation. Morphological changes in HUVECs due to PEF were accompanied by disruption of actin cytoskeleton, loss of tight junction protein—ZO-1 and VE-Cadherin at cell junctions and partial translocation into the cytoplasm. Uptake of propidium iodide (PI) in PEF treated conditions is less than 1% and 2.5% of total number of cells in high voltage (HV) and low-voltage (LV) groups, respectively, implying that BBB disruption to be independent of electroporation under these conditions. 3-D microfabricated blood vessel permeability was found to increase significantly following PEF treatment and confirmed with correlative cytoskeletal changes and loss of tight junction proteins. Finally, we show that the rat brain model can be scaled to human brains with a similar effect on BBB disruption characterized by electric field strength (EFS) threshold and using a combination of two bilateral HD electrode configurations.

Keywords Blood–brain barrier (BBB) disruption · Biological response to electroporation · Low-voltage pulsed electric field · Drug delivery

Introduction

High-voltage pulsed electric fields (HV-PEF) conventionally used for electroporation are known to evoke a plethora of other biological responses in cells and tissues. Temporary disruption of the barrier function in the endothelial layer lining blood vessels is one such off-target biological response observed concurrent to electroporation. Modulation of vasculature by PEF was first reported by Cemazar et al. during electrochemotherapy who suggested that this response may be contributing to overall therapeutic effect [1]. Kanthou et al. determined that PEF stimulates reorganization of the endothelial cell (EC) cytoskeleton which in turn increased microvascular permeability in normal skin and tumors [2–4]. In later work, Markelc et al. identified that alterations in EC–cell gap junction proteins manifests upon exposure to PEF [5]. These PEF-induced responses in vasculature and ECs are transient, where Srimathveeravalli et al. and Kodama et al. [6] demonstrated that the kinetics of blood vessel permeability was independent and longer-lasting than that of cell membrane permeabilization. They

Associate Editor Scott Verbridge oversaw the review of this article.

✉ Govindarajan Srimathveeravalli
govind@umass.edu

Extended author information available on the last page of the article

Published online: 28 April 2023

further demonstrated that PEF mediated vascular changes can promote the delivery of therapeutic agents to tumors, improving therapeutic efficacy in preclinical studies with potential applications to diseases affecting the brain [7].

The blood vessels (capillaries and post capillary venules) of the brain forms a continuous non-fenestrated structure that restricts the contents of the blood plasma from entering the brain parenchyma and thus acting as a barrier [8, 9]. This biological interface consisting of ECs lining the blood vessels, pericytes wrapped around the basement membrane and astrocytes extending their feet to make contact with ECs on the abluminal side, is termed as the blood–brain barrier (BBB) [10]. While BBB integrity is crucial for healthy brain function, this barrier limits the passage and delivery of therapeutic drugs for treating brain tumors and disorders of the central nervous system (CNS) such as Alzheimer, and Parkinsons disease [11, 12]. The impact of PEF and potentially electroporation in altering BBB permeability was first suggested by Lopez-Quintero et al. based on their in vitro work studying deep brain stimulation relevant waveforms in EC monolayers [13]. Hjouj et al., and Garcia et al. simultaneously reported studies on delivery of PEF with invasive needle electrodes for BBB disruption in normal rat brain [14, 15]. Sharabi et al., reported that the use of a "point source" approach, that is, a needle electrode with an extremely short exposure length enabled BBB disruption while reducing ablation of brain tissue by irreversible electroporation [16]. BBB disruption could be transiently achieved in larger volumes of the brain [17]. This group also reported that such BBB disruption was therapeutically relevant, increasing the transport of drugs to the brain, prolonging animal survival [18]. As monophasic PEF conventionally used for electroporation can cause significant neuromuscular activation, Latouche et al. investigated the use of high frequency PEF to treat canine brain tumors that simultaneously produced BBB disruption in canine patients and in healthy rat brain [19–21]. Shu et al. recently demonstrated that there may be further cell-lineage specific effects while using high frequency PEF, with greater impact on the viability of malignant cells in comparison to EC lines [22].

This substantial body of preliminary work on BBB disruption with PEF had two crucial factors that could limit translation to humans. The first was the use of an invasive needle electrode for PEF delivery, rendering this approach infeasible in patients with non-malignant, neurological disorders. Moreover, BBB disruption thus far was only reported while using high voltage PEF. Sharabi et al., performed crucial in vitro and in vivo studies where it was shown that BBB disruption could be achieved even while using low-voltage pulses, where pulse application was performed non-invasively using caliper electrodes typically used to deliver PEF to subcutaneous tumors during electroporation treatments [23, 24]. Building upon this foundation of work, our objective was to determine whether non-invasive BBB disruption with PEF can be accomplished with clinically relevant devices used in patients with neurological conditions, and whether the technique would prove scalable for future use in humans. We also seek to identify whether EC response to PEF was dependent on electroporation phenomenon. In this work, we tested whether head mounted electrodes used for transcranial direct current stimulation (TDCS) applications can evoke BBB disruption in a rat model, using computational models to understand scalability to human head. We then performed in vitro studies to uncover putative mechanisms underlying PEF-induced EC barrier function disruption, and whether such effects dependent on electroporation (Fig. 1).

Materials and Methods

Cell Culture

Primary human umbilical vein endothelial cells (Lonza, Cat # C2519A) were cultured in 10 cm tissue culture plates using endothelial growth media (Lonza, Cat # 3156 & 4147) supplemented with hydrocortisone, hFGF-B, VEGF, R3-IGF-1, ascorbic acid, hEGF, 2% fetal bovine serum (FBS), heparin, gentamicin, and amphotericin-B, maintained in a humidified incubator at 37 °C and 5% CO_2. Cells were allowed to reach 80–90% confluence prior to harvest using 0.05% trypsin–EDTA solution, followed by neutralization with fresh media and centrifuged at 1200 rpm for 5 min. Cells were sub-cultured at 1:4 ratio, passaged every 5 days with cultures between passages 7 and 10 used for studies.

PEF Treatment of Adherent Cells

Silicone gaskets (Grace BioLabs, Cat # 103230) were attached to PLL coated glass slides for PEF treatment of adherent cells. Each gasket chamber well was seeded with 25,000 cells, then allowed to grow until a confluent monolayer was formed. A custom built 4 mm gap parallel plate aluminum electrode setup was placed inside the well (Fig. 5I) and PEF were applied using a BTX 830 generator (Harvard Apparatus). PEF application was performed by varying the voltage and the number of pulses applied (HV: 1000 V/cm, 1–6 pulses; LV-1: 500 V/cm, 40, 60 or 80 pulses; LV-2: 250 V/cm, 400 or 600 pulses) with a fixed pulse width of 100 µs, delivered at 1 Hz frequency.

Cell Viability and Proliferation

Dual staining with propidium iodide (PI, red; dead or reversibly electroporated cells; Thermo Fisher) and Calcein-AM (green; viable live; Thermo Fisher) was used to identify

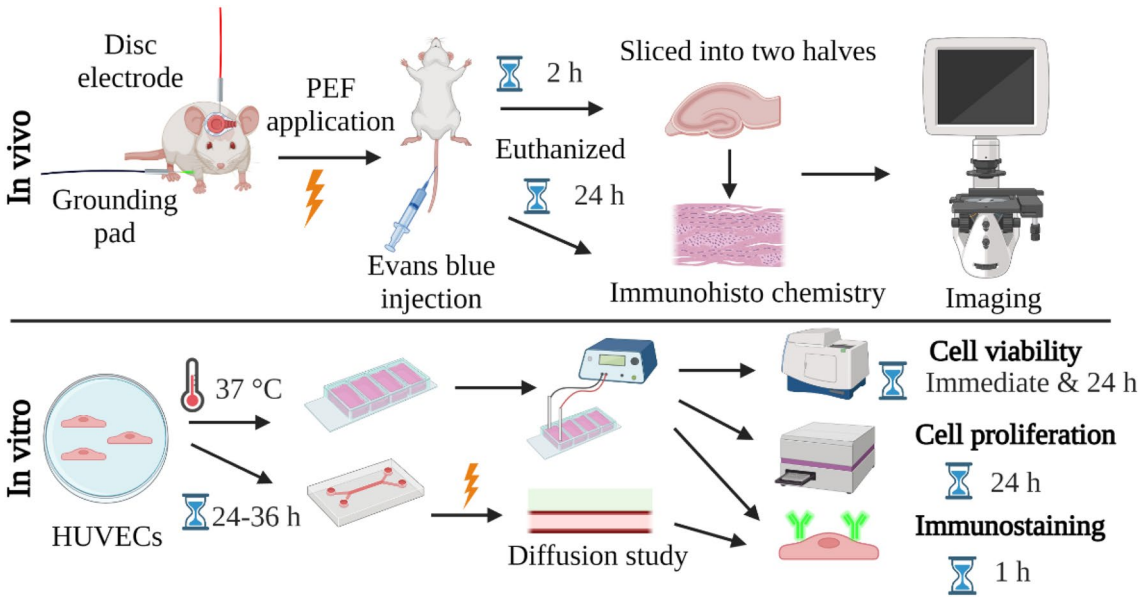

Fig. 1 Overview of in vivo and in vitro experiments with major timepoints and assessments performed

the effect of PEF treatment using automated cell counting with a microscope. Prior to PEF application, 70 µL of fresh media containing 0.33 µL of PI (1 mg/mL) was added to each well. Following brief incubation, the cells were washed and received fresh media containing Calcein-AM (2 µL per mL of media) and Hoechst 33342 (0.3 µg/mL), and further incubation for 10 min. Cells were washed twice with PBS 1 × and replaced with fresh media and the chamber wells were imaged using an automated microscope (ImageXpress Pico, Molecular devices) at × 4 magnification. The cell viability was assessed immediately post-PEF and at 24 h for each pulse parameter combination. Cell proliferation was assessed using cell-counting kit (CCK-8) at 24 h post PEF. Briefly, each chamber well was replaced with fresh media containing 10% of CCK-8 reagent and incubated for 2 h. The media from the chamber wells were transferred to 96-well plates and absorbance was measured at 450 nm using a microplate reader (SpectraMax iD3, Molecular Devices).

Immunofluorescence Staining

Staining was used to visualize PEF mediated changes to actin cytoskeleton and tight junction protein (ZO-1) at 1 h post-PEF application. Briefly, PEF treated and control cells were fixed using 4% paraformaldehyde buffer for 15 min and washed twice with PBS 1 ×, permeabilized using 0.1% Triton-X 100 for 10 min and washed thrice with PBS 1 ×. The cells were then blocked with 1% BSA for 30 min. Blocking buffer was replaced with the staining solution containing Cell Tracker Actin Deep Red (Cat # A57245, Thermo Fisher), Alexa fluor 594 monoclonal ZO-1 antibody (2 µg/mL; Cat # 339194, Thermo Fisher), Alexa Fluor 488 monoclonal VE-Cadherin antibody (4 µg/mL; Cat# SC9989 AF488, Santa Cruz) and Hoechst 33342 (0.3 µg/mL; Cat # PI62249, Thermo Fisher) in 0.1% BSA solution, and was incubated for 90 min. The staining solution was removed and washed thrice with 1 × PBS. Finally, prolong diamond antifade mountant (Cat # P36970, Thermo Fisher) was added to the glass slide prior to mounting the coverslip. The slides were imaged using an automated imaging system (ImageXpress Pico, Molecular devices) at 20X magnification.

Microfluidic Device Fabrication and Setup

A master mold for a microfluidic chip representing a cerebral arteriole (300 µm) was printed in VeroWhite using Stratasys Connex 350 [25]. The mold was used to create a PDMS (elastomer to curing reagent ratio of 10:1) device which was bonded to a glass microscope slide by plasma treatment. The device was autoclaved, following which the surface of glass and PDMS were functionalized by coating the channels and ports with 0.1% PLL solution for 4 h at 37 °C. The device was then washed thrice with 1 × PBS and 1% glutaraldehyde, followed by incubation for 15 min. The device was washed to remove any traces of glutaraldehyde and soaked in 1 × PBS overnight while placed on a rocker. Two 1/32-in. stainless steel pins were used as electrodes (1 cm gap) for PEF application. A 300 µm acupuncture needle was used as a negative mold to create a vascular channel using collagen solution (3 mg/mL). HUVECs in FBS were seeded into the micro channel at a density of 2.5×10^7 cells/mL once the collagen polymerized (Fig. 7A). The device was placed in

a petri dish and fresh endothelial growth media was added until the device was completely immersed. The cells were incubated for 24–48 h until they formed a confluent monolayer in the channel.

PEF Treatment and Permeability Measurement

The permeability of the vessel was quantified using small molecule based fluorescent dyes (FITC-dextran 10 kDa and Rhodamine-dextran 70 kDa; both at 100 µg/mL) once a confluent micro vessel was observable on bright field imaging. The device was prepared for the diffusion study by washing it once with PBS to remove any cell debris. Phase contrast images were acquired immediately prior to addition of the dye solutions. Time lapse imaging was initiated immediately after adding 50 µL of dye solution to the micro vessel via the media port. Images were captured every 30 s for 10 min using a confocal inverted fluorescent microscope (Nikon TiE-HCA). The dye solution was removed, and the device was washed twice with PBS 1 × for 5 min. Fresh media was added to the channel and incubated for 20 min before applying PEF. The diffusion study was repeated immediately after applying PEF. The two electrodes already present in the microfluidic device were connected to the BTX generator to apply PEF across the microfluidic channel. The following parameters were applied to study the effect of PEF on the permeability of the channel: (i) 500 V/cm, 100 pulses, 100 µs, 1 Hz, 1 cm gap between electrodes; (ii) 250 V/cm, 600 pulses, 100 µs, 1 Hz, 1 cm gap between electrodes. After the diffusion studies were performed, the cells were fixed, permeabilized and stained for actin, ZO-1 and VE-Cadherin as mentioned above. The vessels were imaged using Nikon FN1 stand with A1HD resonant scanning multiphoton confocal microscope at a 4 µm step size for a total range of 400 µm.

ImageJ Analysis

Microscopy images were analyzed using ImageJ. The time lapse images obtained from respective filter sets were imported separately as virtual stacks into ImageJ. The vessel and tissue regions were traced individually and the mean fluorescence intensity for each region was calculated for each frame. The mean fluorescence intensity versus time was plotted and the slope was calculated from it.

In Vivo Experiments

Following techniques in a protocol approved by the Institutional Animal Care and Use Committee (IACUC), Sprague Dawley rats ($n = 54$, male) weighing 300–350 g were used in this study. The rats were divided into sham and PEF treatment groups. In the treatment group, 16 different PEF parameters (Voltage 1000, 1500 V; Pulse numbers 10, 100; Pulse width 20, 100 µs; Frequency 1, 10 Hz) were tested in each cohort ($n = 3$ rats). A 1.5-in. midline scalp incision was made from the frontal bone to lambda and a 0.7 cm diameter, 0.2 cm thick cylindrical flat electrode (BioMed, Inc.) was placed above the midline between the Bregma and lambda. The electrode was secured using dental cement and connected to a BTX generator (Harvard Apparatus). A 5 cm × 5 cm grounding pad (Grounding Pad, Bovie Medical) was placed on the abdomen of the animal for use as the return electrode. Control rats underwent all steps in the procedure except application of PEF. Tail vein injection of Evan's blue solution was performed immediately post-PEF was used to assess BBB permeability. A cardiac flush was performed with normal saline 2 h post EB injection to remove any excess dye in the brain and the rats were euthanized using carbon dioxide and bilateral thoracic puncture. A subset of animals treated with the highest energy dose were (1500 V, 100 pulses, 100 µs, 10 Hz) survived 24 h ($n = 3$) to assess clinical evidence of neurological changes. Needle-based PEF delivery was performed as positive control for understanding trauma to the brain when compared to non-invasive PEF application. A 25G needle was placed centrally within a single hemisphere of the brain using stereotactic guidance in Sprague Dawley rats ($n = 2$). PEF were delivered with a single parameter set (500 V, 8 pulses, 100 µs, 1 Hz), reflecting commonly used reversible electroporation protocols. The grounding pad was used as the return electrode. EB injection was not administered in these animals. The animals were euthanized at 2 h post-PEF application following steps used for the non-invasive cohort.

BBB Disruption Efficacy Evaluation

Brains were harvested from skull and were sectioned frontally along the location of the electrode into two halves. Both brain halves samples were exposed flat on the surface and imaged with a handheld camera to quantify the distribution of EB dye in the brain. The brain sections were fixed in formalin and were stained with H&E and TUNEL (cell death) for histologic analysis.

Computational Model Setup

Magnetic resonance imaging (MRI) scans of a rat and human head were segmented into nine tissue masks namely scalp, skull, cerebrospinal fluid (CSF), gray matter, white matter, cerebellum, hippocampus, thalamus, and air to develop a high resolution (rat: 0.1 mm and human: 1 mm) MRI derived finite element method (FEM) model in Simpleware (Synopsys, Inc., CA, USA) using both automatic and manual filters [26–28]. Computer aided design (CAD) model of electrodes of relevant shapes and dimensions were modelled in

SolidWorks (Dassault Systemes Corp., MA, USA) and later imported into Simpleware (Synopsys, CA, USA) for positioning. Specifically, for both human and rat models, two different types of electrodes were modelled: (i) human—small disc electrode (3.2 cm diameter × 0.1 cm thickness) and large disc electrode (5.1 cm diameter × 0.1 cm thickness); (ii) rat—small disc electrode (0.6 cm diameter × 0.1 cm thickness) and square conductive adhesive pad (1.9 × 1.9 cm^2). In human brain model, a bilateral 4 × 1 high definition (HD) montage with a large anode over the right motor cortex and four "return" electrodes (cathode) over the contralateral hemisphere was adapted, whereas in the rat brain model, small disc electrode (anode) was positioned over the exposed skull and the cathode pad was applied over the thoracic region. A small amount of conductive electrolyte gel was assumed to be present at the tissue-electrode interface. An adaptive tetrahedral mesh of the human and rat model resulting from multiple mesh refinements was generated using a voxel-based meshing algorithm and contained > 5.9 million and > 32 million tetrahedral elements, respectively for rat and human models. An isotropic average electrical conductivity (S/m) values for both human and model were assigned as, scalp: 0.465 S/m; skull: 0.01 S/m; CSF: 1.65 S/m; air: 1×10^{-15}; gray matter: 0.276 S/m; cerebellum: 0.276 S/m; hippocampus: 0.126 S/m; white matter: 0.126 S/m; thalamus: 0.276 S/m, electrolyte: 4 S/m; and electrode: 5.99×10^7 S/m. All values were based on prior literature [27, 29]. The volumetric meshes were later imported into COMSOL Multiphysics 5.5 (COMSOL, Inc., MA, USA) to solve the model computationally using Laplace current flow field equation ($\nabla(\sigma \nabla V) = 0$, where V = potential and σ = conductivity) [30].

Boundary and Initial Conditions

The boundary conditions were applied as electric potential at the exposed surface of the anode (human: large electrode over right motor cortex and rat: epicranial disc electrode) and ground at the exposed surface/s of the cathode (human: four "return" electrodes on the contralateral motor cortex and rat: square pad). All remaining external boundaries of both models were electrically insulated. In the human FEM model, 100 pulses at 1500 V were simulated. In a second simulation, the voltage at electrode was increased to meet the BBB disruption threshold within the brain. In the rat model, first the initial conductivity of the tissue was adjusted based on experimental pre-pulse current with an applied potential of 100 V. Then, the experimental post-current values were used to determine the change in impedance before and after treatments. A dynamic conductivity (conductivity as a function of electric field, represented by a sigmoid function [31]) approach was implemented to account for change in tissue conductivity from passage of current [32–34]. Electric potentials delivered at 1000 V and 1500 V with 10 pulses and 100 pulses were modeled. Total charge density delivered at the brain region of interest, electric fields with superimposed field isolines, and current densities for each intensity were predicted and the corresponding values were reported.

Statistical Analysis

All experimental data were recorded as mean ± standard deviation. For all grouped data involving more than one dependent variable, ordinary two-way ANOVA test was performed along with Tukey's multiple comparison test to find the significance between individual test conditions. Kruskal–Wallis test was performed on datasets that did not follow a normal distribution and dependent on a single variable. A p-value of < 0.05 between experimental groups was considered to be statistically significant. All statistical tests were carried out using GraphPad Prism 7.0 (GraphPad, San Diego, USA).

Results

PEF Application with Non-invasive Electrodes in Rats Disrupts the BBB Without Permanent Injury to the Brain

We performed an in vivo dose escalation study by varying the voltage, frequency, pulse width and pulse numbers applied and studying the corresponding distribution of EB dye in the rat brain. In general, higher energy delivered corresponded with a larger region of the brain undergoing BBB disruption. Amongst PEF parameters, increasing the voltage, the number of pulses applied, and the pulse width all seemed to independently increase the region of BBB disruption (Fig. 2A–C, Supplementary Fig. 1). PEF application at 1500 V, 100 µs 100 pulses at 10 Hz produced maximum region of BBB disruption (Fig. 2G). When PEF were delivered at 1000 V, the area of BBB disruption showed little change in response to other pulse parameters (Fig. 2D, E). Interestingly, excepting one parameter set—1500 V and 20 µs (Fig. 2F), pulse application at 10 Hz produced better results than 1 Hz. All animals were recovered following PEF application, where animals sacrificed at 24 h post-treatment did not demonstrate any overt neurological damage as determined by changes in grooming and feeding habits. Examination of brains from animals sacrificed at 2 h post-PEF application demonstrated focal regions of spongiosis of the cerebral cortex and white matter in the medial dorsal portion of the brain in some animals ($n = 6$), which was interpreted as an effect caused by treatment (Fig. 3E, 3F). Such gross changes were largely restricted to animals that received PEF at 1000 or 1500 V, 100 pulses, 100 µs, 10 Hz.

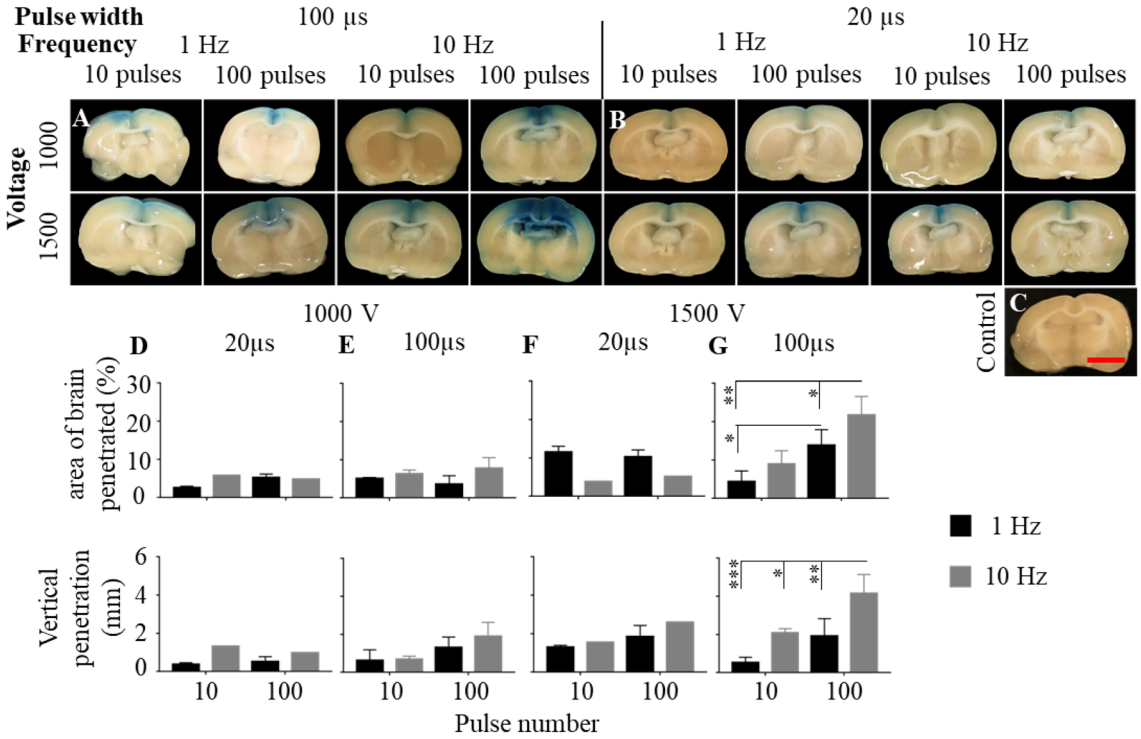

Fig. 2 Effect of PEF on BBB disruption in in vivo rat brain models visualized through tail-vein injection of EB dye and extracting brain slices 2 h post treatment. The experiment groups were divided into groups pertaining to two different pulse widths—**A** 100 µs and **B** 20 µs and **C** control (no treatment). Each treatment group has been treated using two voltages (1000 and 1500 V), two pulse numbers (10 and 100 pulses) and two frequencies (1 and 10 Hz). The vertical penetration depth and % area of brain penetration of EB dye has been quantified and plotted for 1000 V—20 (**D**) and 100 µs (**E**) and 1500 V—20 (**F**) and 100 µs (**G**). *Scale bar* 5 mm; $*p<0.033$, $**p<0.002$, $***p<0.0002$, $****p<0.0001$

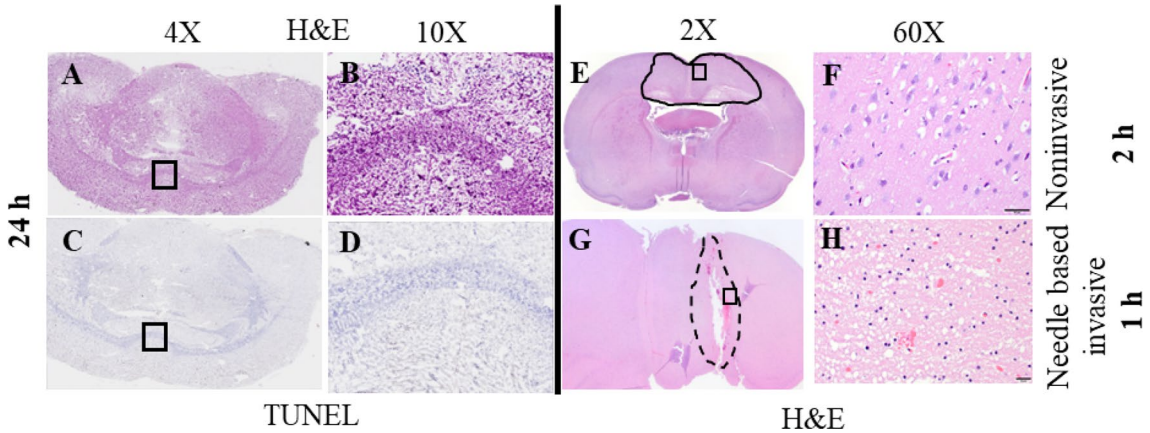

Fig. 3 Histological evaluation of sectioned and paraffin embedded tissue specimens for hematoxylin and eosin (H&E) and TUNEL stains. Rat brain samples in 1500 V, 100 µs, 100 pulses and 10 Hz treatment group were allowed to survive for 24 h, sacrificed, tissues processed and stained for H&E (**A** and **B**) and TUNEL (**C** and **D**) to visualize tissue structure and cell death (brown staining, not prominent) due to PEF treatment. H&E staining was performed at an acute timepoint (1 or 2 h) to visualize changes at the cell/tissue level due to PEF using a needle-based invasive (**G** and **H**) and skull mounted noninvasive methods (**E** and **F**). Black square indicates region of interest and corresponding enlarged images are shown on the right side at higher magnification. The region of treatment effect is marked using solid lines for skull mounted noninvasive group and dotted lines for needle based invasive group in **E** and **G**, respectively

H&E-stained sections from animals sacrificed at 24 h post-PEF application did not demonstrate any abnormal regions in the brain suggesting that PEF-related tissue changes were transient (Fig. 3A, B). Multifocal, minimal TUNEL staining of the meninges was observed in some animals ($n=3$) but was not observed in the control (untreated) animals (Fig. 3C, D). There was no apparent TUNEL staining in the cerebral cortex or white matter, with no evidence of tissue necrosis. In contrast, PEF applied on rat brains using a needle-based approach and sacrificed acutely at 1 h post treatment showed acute necrosis of the frontal cortex and white matter characterized by nuclear pyknosis, vacuolation of neutrophils, vascular hyperemia, and hemorrhages (Fig. 3G, H).

Regions of BBB Disruption in Rat Brain Correlates with Sub-electroporation Field Strength Values

We performed correlative simulation modeling to understand the electric field distribution underlying BBB disruption in rat brain. The electrode montage, electric field isoline plots illustrating field distribution across brain tissues and predicted electric field plots (volume) of the rat model are illustrated in Fig. 4A, B. The electric field distribution corresponding EB-stained rat brain slices for four different voltage—pulse number combinations are also shown (Fig. 4C, D for 1000 V and Fig. 4E, F for 1500 V). All plots were scaled to a peak electric field for each condition and the isoline contour corresponding to the BBB disruption was estimated. We observed that for both voltage conditions, the peak electric field in the tissue varied as a function of number of electric pulses delivered, ranging from (71–127 V/cm) for 1000 V and (196–205 V/cm) for 1500 V for the 10 and 100 pulse conditions, respectively. For both voltage conditions, we found the isoline 63 V/cm closely estimated the areas showing EB deposition in the brain.

Low-Voltage PEF Parameters Produce Morphologic and Gap Junction Protein Alterations in HUVEC Monolayers

We performed an in vitro study to recapitulate our in vivo finding of BBB disruption at pulse parameters at the sub-electroporation threshold. Treatment of HUVEC at 1000 V/cm at increasing pulse numbers gradually reduced cell viability, where treatment with 2 and 3 pulses (termed HV) produced dramatic alterations to cell morphology (Fig. 5A–D) without appreciable reduction in viability or evidence of electroporation based on PI uptake (less than 1% of cells). Using this as a positive control and baseline, we then tested treatment at 500 V/cm and 250 V/cm while increasing pulse numbers in a roughly 1:10 ratio. We found that treatment with 40 or 60 pulses at 500 V/cm and 400 or 600 pulses at 250 V/cm (termed LV) produced similar morphologic changes (Fig. 5E–H) observed at 1000 V/cm and 2 pulses, without reduction in cell viability or evidence of electroporation based on PI uptake (less than 2.5% of cells). HUVEC treated at these electric field and pulse number combination were observed to return to baseline confluence by 24 h without remarkable alterations in cell proliferation as measured by CCK-8 assay. We performed experiments to further probe and understand the intracellular changes due to PEF treatment that

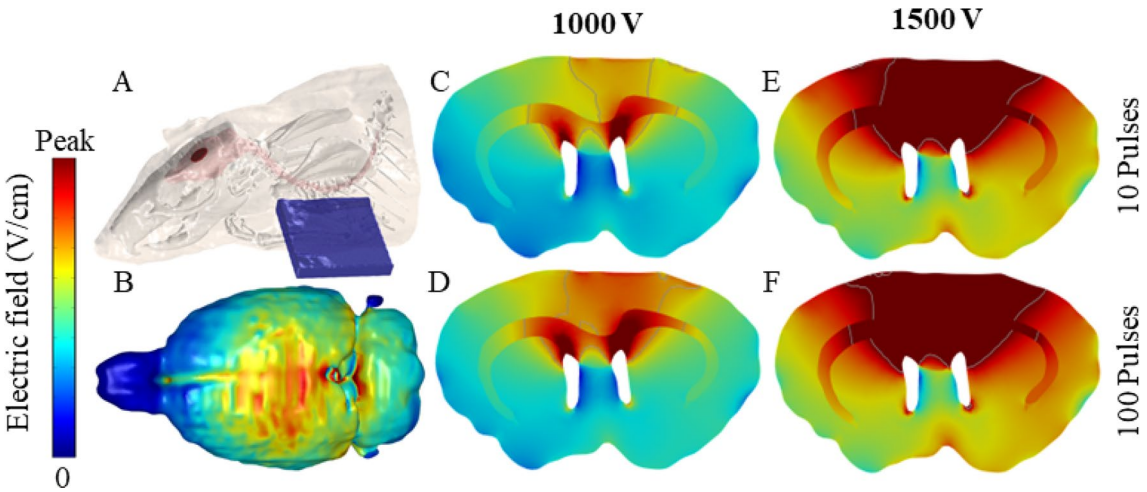

Fig. 4 In silico FEM models of rat brains to determine EFS delivered around the region of dye penetration. **A** An electrode assembly over the brain target. **B** Predicted electric field at the brain for 1500 V 100 pulses treatment group. **C** and **D** illustrate with predicted electric field and the extent of BBB disruption via contour isolines (Contour isoline value: 63 V/cm) at different levels on the same slice plot for 1000 V with 10 (Peak EFS: 71 V/cm) and 100 (Peak EFS: 127 V/cm) pulses, respectively. Similarly, **E** and **F** correspond to 1500 V with 10 (Peak EFS: 196 V/cm) and 100 (Peak EFS: 205 V/cm) pulses, respectively

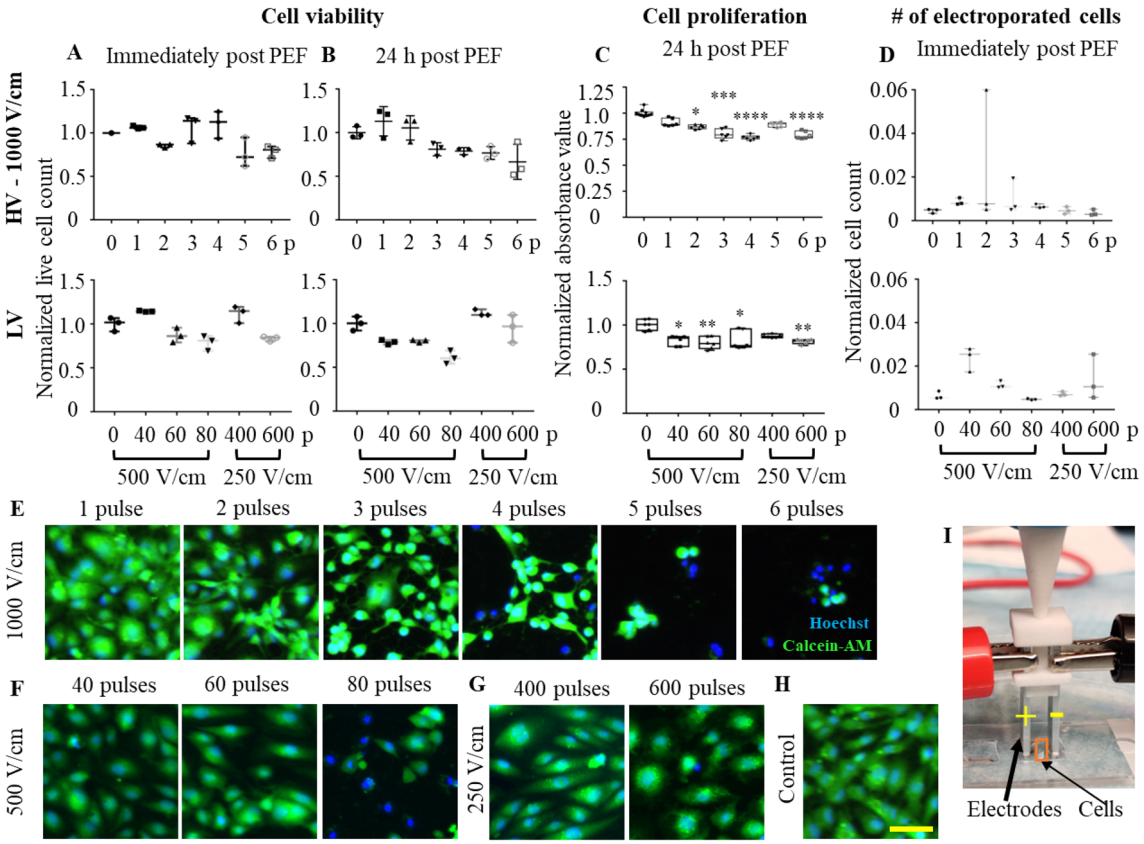

Fig. 5 Dose escalation response of HUVECs to LV and HV-PEF treatments quantified using cell viability, proliferation, and morphological assays. Cell viability was quantified using Calcein-AM and Hoechst stains at two different time points—**A** immediate and **B** 24 h post treatment. Cell proliferation was quantified using CCK-8 and evaluated at **C** 24 h post treatment. **D** The ratio of number of electroporated cells to total number of live cells in control group was quantified using PI, Calcein-AM, and Hoechst stains immediately post treatment for both LV and HV groups. **E**–**H** Morphological changes observed in cells immediately post-PEF treatment in both LV and HV groups stained using Calcein-AM and Hoechst. The 2-D in vitro PEF treatment model is shown in **I** where cells are plated on PLL coated glass slides and treated using custom made electrode insert (4 mm gap) through a BTX generator. *Scale bar* 50 µm; $*p < 0.033$, $**p < 0.002$, $***p < 0.0002$, $****p < 0.0001$

might cause BBB disruption. Immunofluorescent staining was carried out for cytoskeletal protein—actin and tight junction proteins—VE-Cadherin and Zonula Occludens-1 (ZO-1) on 1000 V/cm—2 and 3 pulses (Fig. 6: 2A–E and 3A–E), 500 V/cm 60 pulses and 250 V/cm 600 pulses (Fig. 6: 4A–E and 5A–E) conditions at 1 h post treatment. The actin cytoskeleton in the treated condition showed remodeling and accumulation around the cell periphery when compared to control (Fig. 6: 1A–E) where distinct actin filaments can be seen. We observed a gradual decrease in the presence of VE-Cadherin and ZO-1 at the cell junctions, partial internalization, and localization around the cell nucleus in the treated group compared to control. This resulted in gap formation between cells and disruption of endothelial monolayer. The internalization of tight junction protein was observed more in the LV group than HV whereas actin remodeling effect was stronger in the HV conditions (1000 V/cm 3 pulses) than LV.

Disruption of HUVEC Monolayers by LV-PEF Increases Microvascular Permeability

LV-PEF parameters inducing alterations in HUVECs were tested to see if they could increase microvascular permeability in a microfluidic chip model. A microfluidic device was fabricated as shown in Fig. 7A with a vessel size of 300 µm and seeded with HUVECs and allowed to form a monolayer for permeability studies. The morphological changes in cells before and after PEF treatment are depicted in Fig. 7B. Two different small molecule fluorescent dyes—FITC dextran 10 kDa and Rhodamine dextran 70 kDa were perfused before and after PEF treatment to quantify the percentage increase in permeability (Fig. 7C–F). We observed that the permeability increased by 10 kDa: 44% and 80% and 70 kDa: 22% and 68% for 500 V/cm 100 pulses and 250 V/cm 600 pulses, respectively, following PEF treatment. The rate of diffusion in terms of the change in mean fluorescence

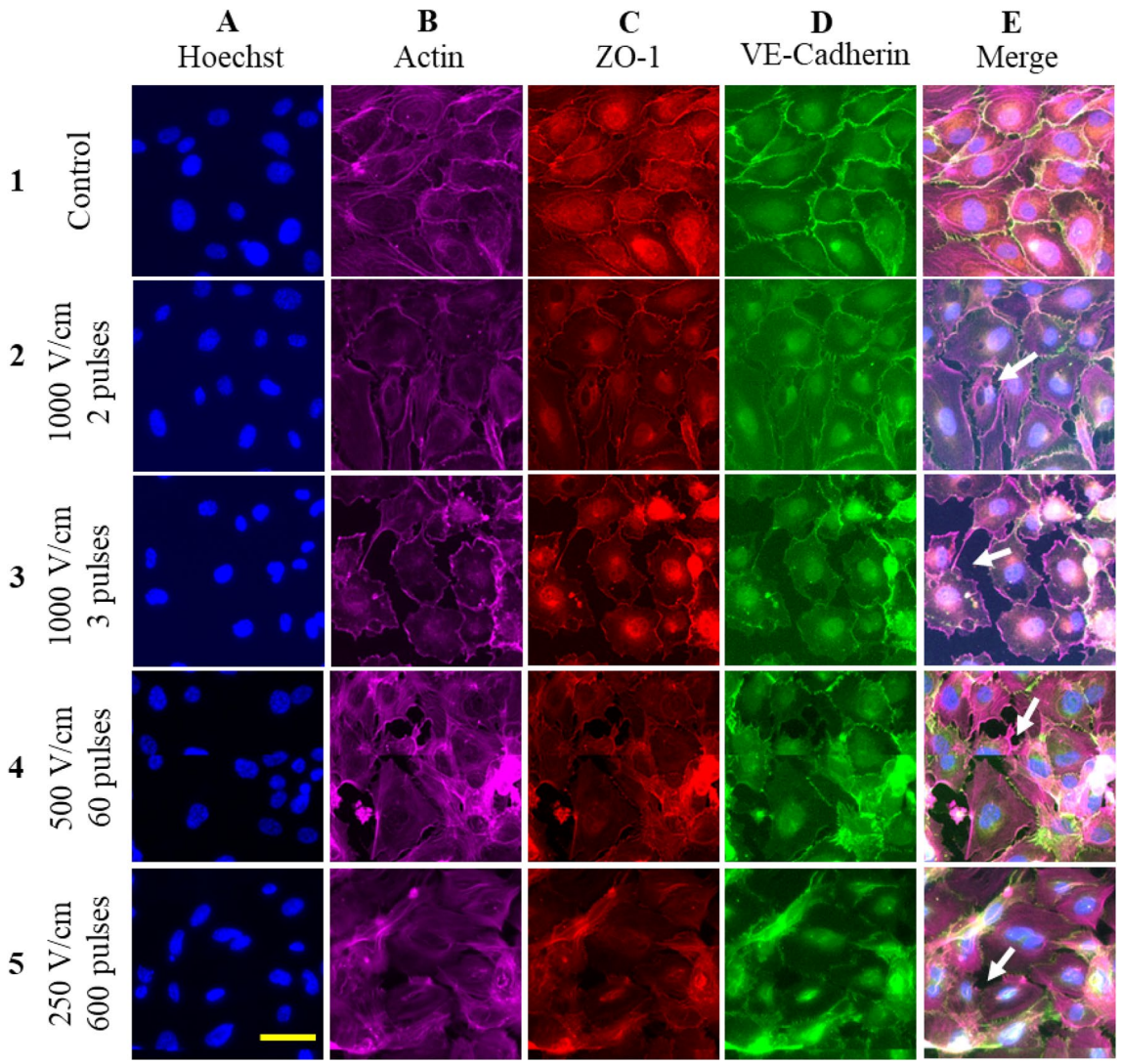

Fig. 6 Immunofluorescence staining of HUVECs following PEF treatment to visualize changes in the actin cytoskeleton and tight gap junctions—VE-Cadherin and ZO-1 at 1 h post treatment. Actin remodelling and tight gap junction disruption and internalization due to PEF treatment can be observed in 1000 V/cm—2 (**2A–E**) and 3 (**3A–E**) pulses indicated by white arrows compared to control (**1A–E**) where VE-Cadherin and ZO-1 are present only at the cell periphery. A similar effect was observed at LV groups—500 V/cm 60 pulses (**4A–E**) and 250 V/cm 600 pulses (**5A–E**). *Scale bar* 50 µm

intensity over time was higher for 10 kDa dye compared to 70 kDa. Immunostaining for actin, VE-Cadherin, and ZO-1 recapitulated key findings observed in HUVEC monolayers (Fig. 7G), confirming the mechanism that may underlie LV-PEF mediated BBB disruption.

Rat Brain Simulations Can Be Scaled to Human Brains and Have a Similar Effect on BBB Disruption

To illustrate the scalability of noninvasive electrode approach to induce BBB disruption using PEF application in humans [35, 36], we matched the BBB disruption threshold in the rat brain by adjusting the applied voltage to 1972 V using a HD TDCS electrodes assembled in a bilateral fashion (anode over right motor cortex and four cathodes on the contralateral hemisphere) over the targeted brain region (Fig. 8A). The electric field intensity levels reached irreversible electroporation thresholds in the scalp (peak: 385.99 V/cm, Fig. 8B) and the skull (peak: 1707.3 V/cm, Fig. 8C) but note in the brain (peak: 40 V/cm, Fig. 8D–F). The maximum field intensity was reached at approximately 18.6 mm from the electrode interface and was concentrated in regions of brain folding. Subsequently we increased the stimulation voltage to 3106.5 V/cm to produce electric field strengths of 63 V/cm within the brain, with corresponding doubling of field strength within the skull and scalp.

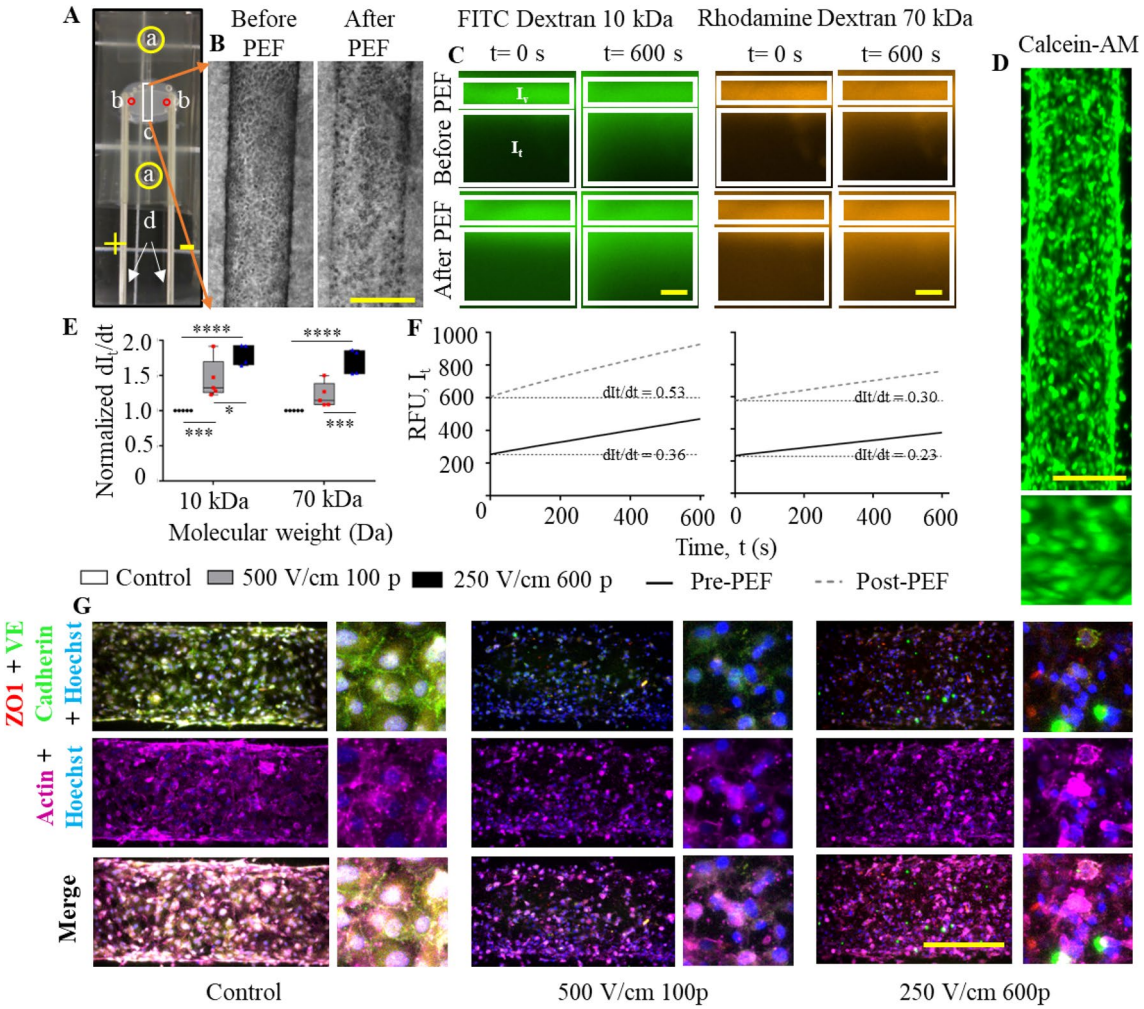

Fig. 7 Effect of PEF treatment on permeability and cytoskeleton and TJ protein changes in 3-D in vitro microfluidic blood vessel model. The microfluidic chip design is shown in **A** where **a** (yellow circle) and **b** (red circle) denotes the media and ECM port, respectively, **c** (white rectangle) shows the lumen region where cells are present, and **d** shows the electrode positions in the chip (depicted by arrows). **B** Phase contrast images of cells in lumen before and after PEF. **C** Dye diffusion rate across confluent monolayer of cells assessed using fluorescently tagged dextran 10 kDa (FITC) and 70 kDa (Rhodamine) before and after PEF treatment for 10 min. I_v vessel intensity; I_t tissue intensity. **D** Live cell imaging performed using Calcein-AM to visualize a confluent monolayer of cells in the blood vessel. **E** The rate of change of mean fluorescence intensity quantifies the rate of diffusion of the dye across the lumen which is normalized to the value obtained before PEF treatment for each chip. The values are plotted for different treatment groups for both the dyes. **F** The rate of diffusion is plotted, and the corresponding slope value is used for diffusion rate calculations. **G** The cytoskeletal changes and TJ disruption are visualized by staining for actin (magenta), VE-Cadherin (green), ZO-1 (red) and nucleus (blue) for 500 V/cm 100 pulses, 250 V/cm 600 pulses and control groups. *Scale bar* 250 µm; $*p < 0.033$, $**p < 0.002$, $***p < 0.0002$, $****p < 0.0001$

Discussion

Our results confirm the feasibility of inducing BBB disruption in rat brain by PEF delivery using non-invasive electrodes conventionally used for neurostimulation application. PEF delivery with this approach was associated with transient, minimal and reversible alterations in brain ultra-morphology, something that would be unavoidable when using needle electrodes. Correlative simulation models revealed that the electric field strength within regions demonstrating BBB disruption to be substantially lower than what would be necessary for electroporation. We delved into this finding by performing additional in vitro studies to uncover possible mechanisms. We found that PEF evokes actin cytoskeletal remodeling, and translocation of gap junction proteins into the cytoplasm of HUVECs without indication of permeabilization as measured by PI dye uptake. Such biological responses were reproduced at substantially lower electric field strengths, demonstrating a roughly 1:10 relationship between the PEF dose (voltage) to duration (number of pulses). These low-voltage PEF parameters were then shown to increase the permeability of microvasculature in vitro,

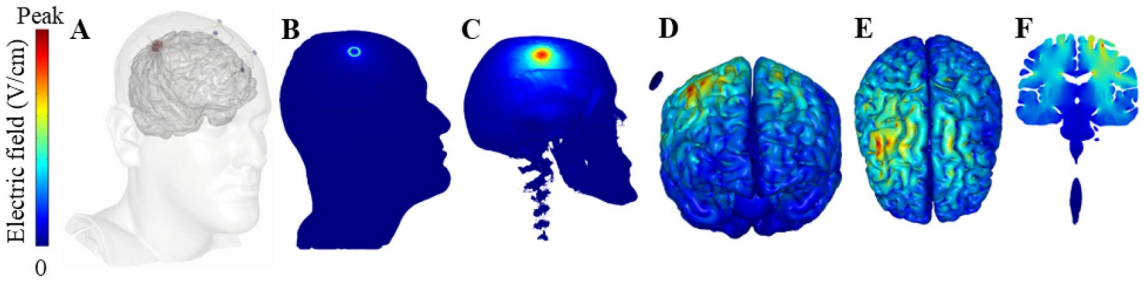

Fig. 8 Feasibility of scaling the in vivo rat brain model to humans for BBB disruption using PEF. **A** An exemplary FEM simulation model representing the usage of PEF in humans using a bilateral 4×1 high definition (HD) montage with a large anode over the right motor cortex and four "return" electrodes (cathode) over the contralateral hemisphere. The electric field distribution on the scalp (**B**), skull (**C**) and brain (**D–F**) at a scaled intensity of 1972 V at 100 pulses is depicted above. The maximum depth of BBB disruption (having a threshold of 63 V/cm) occurred at 18.6 mm from the surface of the electrode (**D**). The peak values of EFS for scalp, skull and brain occur at 3985, 1707 and 40 V/cm, respectively. **E** and **F** show the front and back view of the brain, depicting the EFS distribution

augmenting transport across the endothelial layer. We also demonstrate the concept of BBB disruption in human sized brain using low-voltage PEF delivered with scalp mounted electrodes.

The transport of molecules and material across the capillaries in the brain is tightly regulated by the BBB, a physiologic property that arises from cells of the NVU, namely BEC, neurons, astrocytes, pericytes and vascular smooth muscle cells (*VSMC*) [8, 37, 38]. The BBB supports a healthy brain by regulating the transport of nutrients and waste products while protecting the brain from pathogens and inflammation [39, 40]. Simultaneously, the BBB also impedes the passage of most therapeutic molecules, antibodies and peptides into the brain [41–43], posing a major challenge in the treatment of patients with neurological and oncologic diseases in the brain, underscoring the need to study and improve our ability to modulate its function. BBB disruption in patients and animals undergoing electroconvulsive therapy (*ECT*) was discovered in 1960s [44–46], but further investigation was restricted due to side-effects associated with the technique. In 2010, Bikson et al. identified that PEF used for DBS [47] and static electric fields used for TDCS [48, 49] transiently increases BBB permeability to fluorescent dyes. The three techniques use substantially different PEF waveforms, frequencies, and amplitude, yet all have been shown to produce changes in BBB permeability. These findings are unsurprising as BBB exhibits inherent bioelectric properties, such as the induction of a trans-endothelial electrical resistance arising from the differential ionic flux across the capillary wall, and retrograde transmission of electrical signals along capillary vessels [50].

Similar to what has been reported in neurostimulation applications, PEF conventionally used for electroporation are also known to evoke off-target BBB disruption. The PEF parameters that have been reported to produce this effect span a wide range of values. The key parameters tested in literature are the voltage or electric field, the duration of pulse application as function of number of pulses applied or the pulse width, and the frequency of pulse application. In our preliminary screening experiments, we tested 1000 V/cm while evaluating the minimum number of pulses that evoke cytoskeletal remodeling that is broadly agreed to underlie BBB disruption during PEF application. We found that 2–3 pulses were sufficient to produce this cellular response with minimal evidence of electroporation, consistent with literature where greater number of (5–8) pulses are required to produce reversible electroporation in adherent cells [1]. We then heuristically tested increasing dosing to reproduce cytoskeletal remodeling response while reducing the electric field strength, achieving equivalent outcomes at both 250 and 500 V/cm. These values are somewhat higher when compared to reports by Sharabi et al. who report alterations in monolayer permeability with dose values as low as 7.5–150 V/cm and 10 pulses. Differences in results between our experiments may be explained by the assay used to assess response; in our case we studied cellular response while they assayed monolayer permeability. Subsequent experiments from the same Sharabi group were performed with substantially increased voltage (100–300 V) and pulse numbers (100–400) to produce the BBB disruption in mice. This trade-off is consistent with our experiments where higher energy and dosing is required to achieve BBB disruption in vivo, whereas such energy levels in vitro would prove lethal to cells. As our in vivo experiments preceded in vitro studies, we did not assess low-voltage and high-pulse combinations. Besides voltage, frequency and pulse shape also produced BBB disruption at a wide range of values. Our experiments were performed with monophasic pulses at 1 and 10 Hz while Partridge et al. and Lorenzo et al. have shown that such effects while using high-frequency (burst scheme—5–5–5 µs, 200 bursts) biphasic pulses [21, 51]. Our results, and those from literature suggest that BBB disruption from PEF may largely be independent of electroporation and can be produced using a wide range of PEF parameters.

Lorenzo et al. have demonstrated the feasibility of BBB disruption in rat brain models using high frequency PEF as

early as 1 h through the uptake of gadopentetate dimeglumine and EB dye. The permeability returns to basal levels at 96 h post treatment [20]. We believe BBB disruption from PEF application is mediated by inherent biological response of ECs to electric fields. The cellular responses of actin cytoskeleton remodeling, gap junction loss and translocation and cell morphology changes have been consistently reported to arise following exposure to PEF having variable voltage, duration, and frequency. Partridge et al. showed that high frequency PEF can induce changes in BBB permeability as early as 1 h post treatment. F/G actin ratio decreased immediately post treatment and expression of TJ proteins like Claudin, ZO-1 and Occludin decreased drastically 24 h post treatment and returned to base levels after 72–96 h of treatment [51]. Likewise, Sharabi et al. showed that PEF (5–100 V, 9 mm, 10 pulses, 50 µs) induced transient VE-Cadherin disruption in the LV groups and resulted in an increase in the permeability of EC monolayer at 20 min post treatment and returned to basal level after 24 h [23]. Kanthou et al. and Cecil et al. have also shown that electroporation causes immediate but transient changes in actin and microtubule structures at different PEF parameters [2, 52].

Our study reinforces several findings in the literature while contributing new evidence on the effect and mechanisms by which PEF induces BBB disruption. As an exploratory study, there are several limitations in our experiments. We decided to mount the electrodes in our rat experiments directly on the skull to bypass confounding effects of the skin. We anticipate that having scalp mounted electrodes would still be able to induce BBB disruption, while possibly reducing the volume of BBB disruption. While we did not observe ablative effects in the brain, there may have been cell death within the skull which was not investigated. Our experiments demonstrate BBB disruption at low voltages, but the kinetics were not documented as we did not image the animals and had a single timepoint for assessment. An MRI study can be performed to monitor this effect, with timing of BBB closure and possible differences with kinetics when compared to high voltage PEF. Our in vitro studies were performed on a HUVEC monolayer and not a true BBB model that incorporates astrocytes and pericytes and this choice was motivated by the ability to isolate cellular effects. Although the effects observed in vivo are similar to our in vitro study, the exact mechanism of BBB disruption in vivo has not been explored in this study. Our human-head simulation experiment does not consider localized effects such as the risk of irreversible electroporation directly under the electrode location and thermal effects. The voltage in the human brain model was roughly twice as high as what was required to induce BBB disruption in rat brain. While this may seem excessive, we did not evaluate strength-duration curves in this model based upon our in vitro findings. We anticipate that spatial and temporal distribution of electric field and pulse application over several electrodes may allow induction of BBB disruption over a larger volume in human brain by increasing pulse numbers while reducing the voltage and can potentially target deeper regions of the brain. However, we anticipate achieving precise geometry of BBB disruption deep within human brain would require substantial optimization of pulse delivery strategies and additional technological advancements. The in vivo experiments on rats were performed with a single electrode placed on the skull and the volume of BBB disruption is restricted to the area under it. We anticipate performing additional experiments to address some of these questions in the future.

Conclusion

Dose-wise uptake of EB dye across rat brain tissue shows that BBB disruption using skull mounted non-invasive disc electrodes is feasible. Simulation results predicted that disruption of BBB happens at low EFS, and the total charge delivered increases with increase in voltage and pulse numbers. 2-D in vitro experiments performed showed that cell viability and proliferation decrease with increase in pulse numbers for a given voltage, but cell monolayer disruption is possible at lower pulse numbers while preserving high viability and proliferation. Actin cytoskeletal remodeling and loss of TJ protein was observed in both the 2-D and 3-D models due to PEF treatment causing BBB disruption. Permeability to fluorescently tagged dextran molecules in a microfabricated BV model increases due to the application of PEF compared to control. Simulation results show that the current rat brain model can be scaled to humans obtaining a similar range of EFS and current density for BBB disruption for the same applied voltage. This may serve as a new means to facilitate drug delivery to superficial brain locations in the future.

Supplementary Information The online version contains supplementary material available at https://doi.org/10.1007/s10439-023-03211-3.

Author Contributions Experimental design: GS, NRR; In vitro experiments: NRR; In vivo experiments: WRV, MF, LV, GS; Computational modeling: NK, MB; Data analysis: NRR, WRV, MF, LV, NK, GS; Statistical analysis: NRR, GS; Manuscript preparation: NRR, JJ, GS, MB.

Funding G.S. acknowledges grant and funding support from the National Cancer Institute and the National Institute of Diabetes, and Digestive and Kidney Diseases of the National Institutes of Health under Award Number U54CA137788/U54CA132378, R01CA236615 and R01DK129990, the Department of Defense CDMRP PRCRP Award CA170630, and the Institute for Applied Life Sciences in the University of Massachusetts at Amherst. MB is supported by Grants from Harold Shames and the National Institutes of Health: NIH-NIDA UG3DA048502, NIH-NIGMS T34 GM137858, NIH-NINDS R01 NS112996, NIH-NINDS R01 NS101362, and NIH-G-RISE T32GM136499.

Declarations

Conflict of interest The authors report no relevant disclosures related to the work presented here. The City University of New York has intel-

lectual property (IP) on neuro-stimulation systems and methods with authors NK and MB as inventors. NK is an employee of Synchron, Inc. and consults for Ybrain, Inc. and Ceragem Medical. MB has equity in Soterix Medical, Inc. MB consults, received grants, assigned inventions, and/or serves on the SAB of SafeToddles, Boston Scientific, GlaxoSmithKline, Biovisics, Mecta, Lumenis, Halo Neuroscience, Google-X, i-Lumen, Humm, Allergan (Abbvie), and Apple. G.S. holds stock options in Aperture Medical.

Disclosure Confocal images were imaged in the Light Microscopy Facility and Nikon Center of Excellence at the Institute for Applied Life Sciences, University of Massachusetts Amherst with support from the Massachusetts Life Science Center. The 3-D printed parts and mastermolds were printed using Advanced Digital Design and Fabrication core facility, University of Massachusetts Amherst.

References

1. Cemazar, M., C. S. Parkins, A. L. Holder, D. J. Chaplin, G. M. Tozer, and G. Sersa. Electroporation of human microvascular endothelial cells: evidence for an anti-vascular mechanism of electrochemotherapy. *Br. J. Cancer*. 84(4):565–570, 2001.
2. Kanthou, C., S. Kranjc, G. Sersa, G. Tozer, A. Zupanic, and M. Cemazar. The endothelial cytoskeleton as a target of electroporation-based therapies. *Mol. Cancer Ther.* 5(12):3145–3152, 2006.
3. Corovic, S., B. Markelc, M. Dolinar, M. Cemazar, and T. Jarm. Modeling of microvascular permeability changes after electroporation. *PLoS ONE*. 10(3):e0121370, 2015.
4. Bellard, E., et al. Intravital microscopy at the single vessel level brings new insights of vascular modification mechanisms induced by electropermeabilization. *J. Control. Release*. 163(3):396–403, 2012.
5. Markelc, B., et al. Increased permeability of blood vessels after reversible electroporation is facilitated by alterations in endothelial cell-to-cell junctions. *J. Control. Release*. 276(October 2017):30–41, 2018.
6. Srimathveeravalli, G., et al. Reversible electroporation-mediated liposomal doxorubicin delivery to tumors can be monitored with 89 Zr-labeled reporter nanoparticles. *Mol. Imaging*. 17:1–9, 2018.
7. Kodama, H., et al. Electroporation-induced changes in tumor vasculature and microenvironment can promote the delivery and increase the efficacy of sorafenib nanoparticles. *Bioelectrochemistry*.130:107328, 2019.
8. Richard Daneman, A. P. The blood–brain barrier. *Cold Spring Harb. Perspect. Biol.* 7(1):a020412, 2015.
9. Hajal, C., B. Le Roi, R. D. Kamm, and B. M. Maoz. Biology and models of the blood–brain barrier. *Annu. Rev. Biomed. Eng.* 23:359–384, 2021.
10. Wong, A. D., M. Ye, A. F. Levy, J. D. Rothstein, D. E. Bergles, and P. C. Searson. The blood–brain barrier: an engineering perspective. *Front. Neuroeng.* 6(JUL):1–22, 2013.
11. Luo, H., and E. V. Shusta. Blood–brain barrier modulation to improve glioma drug delivery. *Pharmaceutics*. 12(11):1–12, 2020.
12. Bonakdar, M., P. M. Graybill, and R. V. Davalos. A microfluidic model of the blood–brain barrier to study permeabilization by pulsed electric fields. *RSC Adv.* 7(68):42811–42818, 2017.
13. Lopez-Quintero, S. V., A. Datta, R. Amaya, M. Elwassif, M. Bikson, and J. M. Tarbell. DBS-relevant electric fields increase hydraulic conductivity of in vitro endothelial monolayers. *J. Neural Eng.* 7(1):16005, 2010.
14. Hjouj, M., et al. MRI study on reversible and irreversible electroporation induced blood–brain barrier disruption. *PLoS ONE*. 7(8):1–9, 2012.
15. Garcia, P. A., et al. 7.0-T magnetic resonance imaging characterization of acute blood–brain-barrier disruption achieved with intracranial irreversible electroporation. *PLoS ONE*. 7(11):1–8, 2012.
16. Sharabi, S., et al. Dynamic effects of point source electroporation on the rat brain tissue. *Bioelectrochemistry*. 99:30–39, 2014.
17. Sharabi, S., D. Last, D. Daniels, S. Liraz Zaltsman, and Y. Mardor. The effects of point-source electroporation on the blood–brain barrier and brain vasculature in rats: an MRI and histology study. *Bioelectrochemistry*. 134:107521, 2020.
18. Sharabi, S., et al. The application of point source electroporation and chemotherapy for the treatment of glioma: a randomized controlled rat study. *Sci. Rep.* 10(1):1–12, 2020.
19. Latouche, E. L., et al. High-frequency irreversible electroporation for intracranial meningioma: a feasibility study in a spontaneous canine tumor model. *Technol. Cancer Res. Treat.* 17:1–10, 2018.
20 Lorenzo, M. F., et al. Temporal characterization of blood–brain barrier disruption with high-frequency electroporation. *Cancers*. 11(12):2019, 1850.
21. Lorenzo, M. F., et al. An investigation for large volume, focal blood–brain barrier disruption with high-frequency pulsed electric fields. *Pharmaceuticals*. 14(12):1–22, 2021.
22. Shu, T., et al. Lethal electric field thresholds for cerebral cells with irreversible electroporation and H-FIRE protocols: an in vitro three-dimensional cell model study. *J. Biomech. Eng.* 144(10):1–9, 2022.
23. Sharabi, S., et al. Transient blood–brain barrier disruption is induced by low pulsed electrical fields in vitro: an analysis of permeability and trans-endothelial electric resistivity. *Drug Deliv.* 26(1):459–469, 2019.
24. Sharabi, S., et al. Non-invasive low pulsed electrical fields for inducing BBB disruption in mice—feasibility demonstration. *Pharmaceutics*. 13(2):1–15, 2021.
25 Polacheck, W. J., M. L. Kutys, J. B. Tefft, and C. S. Chen. Microfabricated blood vessels for modeling the vascular transport barrier. *Nat. Protoc.* 14(5):1425–1454, 2019.
26. Datta, A., V. Bansal, J. Diaz, J. Patel, D. Reato, and M. Bikson. Gyri-precise head model of transcranial direct current stimulation: improved spatial focality using a ring electrode versus conventional rectangular pad. *Brain Stimul.* 2(4):201–207, 2009.
27. Edemann-Callesen, H., et al. Non-invasive modulation reduces repetitive behavior in a rat model through the sensorimotor corticostriatal circuit. *Transl. Psychiatry*. 8(1):11, 2018.
28. Hadar, R., et al. Prevention of schizophrenia deficits via non-invasive adolescent frontal cortex stimulation in rats. *Mol. Psychiatry*. 25(4):896–905, 2020.
29. Song, W., D. Q. Truong, M. Bikson, and J. H. Martin. Transspinal direct current stimulation immediately modifies motor cortex sensorimotor maps. *J. Neurophysiol.* 113(7):2801–2811, 2015.
30. Bikson, M., et al. Modeling sequence and quasi-uniform assumption in computational neurostimulation. *Prog. Brain Res.* 222:1–23, 2015.
31. Unal, G., et al. Adaptive current-flow models of ECT: explaining individual static impedance, dynamic impedance, and brain current density. *Brain Stimul.* 14(5):1154–1168, 2021.
32. Neal, R. E., P. A. Garcia, J. L. Robertson, and R. V. Davalos. Experimental characterization and numerical modeling of tissue electrical conductivity during pulsed electric fields for irreversible electroporation treatment planning. *IEEE Trans. Biomed. Eng.* 59(4):1076–1085, 2012.
33. Šel, D., D. Cukjati, D. Batiuskaite, T. Slivnik, L. M. Mir, and D. Miklavčič. Sequential finite element model of tissue electropermeabilization. *IEEE Trans. Biomed. Eng.* 52(5):816–827, 2005.
34 Garcia, P. A., J. H. Rossmeisl, R. E. Neal, T. L. Ellis, and R. V. Davalos. A parametric study delineating irreversible electroporation from thermal damage based on a minimally invasive

intracranial procedure. *Biomed. Eng. Online*. 2011. https://doi.org/10.1186/1475-925X-10-34.
35. Bikson, M., et al. Safety of transcranial direct current stimulation: evidence based update 2016. *Brain Stimul.* 9(5):641–661, 2016.
36. Khadka, N., D. Q. Truong, P. Williams, J. H. Martin, and M. Bikson. The Quasi-uniform assumption for Spinal Cord Stimulation translational research. *J. Neurosci. Methods*.328(September):108446, 2019.
37. Rubin, L. L., and J. M. Staddon. The cell biology of the blood–brain barrier. *Annu. Rev. Neurosci.* 22(1):11–28, 1999.
38. Obermeier, B., R. Daneman, and R. M. Ransohoff. Development, maintenance and disruption of the blood–brain barrier. *Nat. Med.* 19(12):1584–1596, 2013.
39. Tsai, P. S., et al. Correlations of neuronal and microvascular densities in murine cortex revealed by direct counting and colocalization of nuclei and vessels. *J. Neurosci.* 29(46):14553–14570, 2009.
40. Vanlandewijck, M., et al. A molecular atlas of cell types and zonation in the brain vasculature. *Nature*. 554(7693):475–480, 2018.
41. Zheng, X., et al. LC–MS-MS quantitative determination of gefitinib in human serum and cerebrospinal fluid. *Chromatographia*. 74(1–2):41–49, 2011.
42. Tan, J., M. Li, W. Zhong, C. Hu, Q. Gu, and Y. Xie. Tyrosine kinase inhibitors show different anti-brain metastases efficacy in NSCLC: a direct comparative analysis of icotinib, gefitinib, and erlotinib in a nude mouse model. *Oncotarget*. 8(58):98771–98781, 2017.
43. Stemmler, H.-J., M. Schmitt, A. Willems, H. Bernhard, N. Harbeck, and V. Heinemann. Ratio of trastuzumab levels in serum and cerebrospinal fluid is altered in HER2-positive breast cancer patients with brain metastases and impairment of blood–brain barrier. *Anticancer Drugs*. 18(1):23–28, 2007.
44. Rosenblatt, S., J. D. Chanley, H. Sobotka, and M. R. Kaufman. Interrelationships between electroshock, the blood–brain barrier, and catecholamines. *J. Neurochem.* 5(2):172–176, 1960.
45. Bolwig, T. G., M. M. Hertz, O. B. Paulson, H. Spotoft, and O. J. Rafaelsen. The permeability of the blood–brain barrier during electrically induced seizures in man. *Eur. J. Clin. Investig.* 7(2):87–93, 1977.
46. Pudenz, R. H., L. A. Bullara, D. Dru, and A. Talalla. Electrical stimulation of the brain. II. Effects on the blood–brain barrier. *Surg. Neurol.* 4(2):265–270, 1975.
47. Elwassif, M. M., Q. Kong, and M. Vazquez. DBS-relevant electric fields increase hydraulic conductivity of in vitro endothelial monolayers Related content Bio-heat transfer model of deep brain stimulation. *J. Neural Eng.*7(1):016005, 2010.
48. Cancel, L. M., K. Arias, M. Bikson, and J. M. Tarbell. Direct current stimulation of endothelial monolayers induces a transient and reversible increase in transport due to the electroosmotic effect. *Sci. Rep.* 8(1):9265, 2018.
49. Shin, D. W., et al. In vivo modulation of the blood–brain barrier permeability by transcranial direct current stimulation (tDCS). *Ann. Biomed. Eng.* 48(4):1256–1270, 2020.
50. Bahr-Hosseini, M., and M. Bikson. Neurovascular-modulation: a review of primary vascular responses to transcranial electrical stimulation as a mechanism of action. *Brain Stimul.* 14(4):837–847, 2021.
51. Partridge, B. R., et al. High-frequency irreversible electroporation (H-FIRE) induced blood–brain barrier disruption is mediated by cytoskeletal remodeling and changes in tight junction protein regulation. *Biomedicines*. 10(6):1384, 2022.
52. Meulenberg, C. J. W., V. Todorovic, and M. Cemazar. Differential cellular effects of electroporation and electrochemotherapy in monolayers of human microvascular endothelial cells. *PLoS ONE*. 7(12):1–9, 2012.

Authors and Affiliations

Neeraj Raghuraman Rajagopalan[1] · William-Ray Vista[2] · Masashi Fujimori[2,8] · Laurien G. P. H. Vroomen[3] · Juan M. Jiménez[1] · Niranjan Khadka[4,5,6] · Marom Bikson[6] · Govindarajan Srimathveeravalli[1,7]

Neeraj Raghuraman Rajagopalan
nraghuramanr@umass.edu

William-Ray Vista
vistaw@mskcc.org

Masashi Fujimori
fujimori.masashi@gmail.com

Laurien G. P. H. Vroomen
La.vroomen@amsterdamumc.nl

Juan M. Jiménez
juanjimenez@umass.edu

Niranjan Khadka
nkhadka@mgh.harvard.edu

Marom Bikson
bikson@ccny.cuny.edu

[1] Department of Mechanical and Industrial Engineering, University of Massachusetts Amherst, Amherst, MA, USA

[2] Department of Radiology, Interventional Radiology Service, Memorial Sloan-Kettering Cancer Center, New York, NY, USA

[3] Department of Radiology and Nuclear Medicine, Amsterdam UMC, Amsterdam, Netherlands

[4] Division of Neuromodulation, Department of Psychiatry, Massachusetts General Hospital, Harvard Medical School, Boston, MA, USA

[5] Synchron Inc, Brooklyn, NY, USA

[6] Department of Biomedical Engineering, The City College of New York, New York, NY, USA

[7] Institute for Applied Life Sciences, University of Massachusetts Amherst, Amherst, MA, USA

[8] Department of Radiology, Mie University, Tsu, Mie, Japan